

An 18.2%-efficient black-silicon solar cell achieved through control of carrier recombination in nanostructures

Jihun Oh*, Hao-Chih Yuan and Howard M. Branz

Silicon nanowire and nanopore arrays promise to reduce manufacturing costs and increase the power conversion efficiency of photovoltaic devices. So far, however, photovoltaic cells based on nanostructured silicon exhibit lower power conversion efficiencies than conventional cells due to the enhanced photocarrier recombination associated with the nanostructures. Here, we identify and separately measure surface recombination and Auger recombination in wafer-based nanostructured silicon solar cells. By identifying the regimes of junction doping concentration in which each mechanism dominates, we were able to design and fabricate an independently confirmed 18.2%-efficient nanostructured 'black-silicon' cell that does not need the antireflection coating layer(s) normally required to reach a comparable performance level. Our results suggest design rules for efficient high-surface-area solar cells with nano- and microstructured semiconductor absorbers.

Arrays of vertically aligned silicon nanostructures can reduce the volume of semiconductor absorber necessary for high efficiency by providing nearly ideal photon absorption across the solar spectrum. Near-zero reflection over a broad range of incident angles is obtained by forming a density-graded layer with features smaller than the wavelength of light^{1–3}, which eliminates the need for conventional vacuum-deposited antireflection coatings. When the size of surface features equals or exceeds the wavelength of the incident light, nano- and microstructures also provide beneficial light trapping that increases the effective path length in the silicon^{4–6}. To reduce costs, the nanostructures can be directly grown on film layers⁷ or transferred to cheap and/or flexible substrates^{8,9}. The nanostructures can be fabricated by a variety of methods, including vapour–liquid–solid growth^{5,8,10,11}, metal-assisted etching^{2,3,12–14}, reactive ion etching^{4,15,16} and laser modification¹⁷.

Efficient photovoltaic cells also require efficient photoexcited carrier collection from the semiconductor absorber. Photovoltaic cells with arrays of silicon nanowires or nanopores have been fabricated with bulk diffused^{13–16,18,19} or radial p–n junctions for photocarrier collection^{4,8,10–12,19}. Device modelling indicates that nanostructured photovoltaic cells with a radial p–n junction can relax the long minority carrier collection length requirements of conventional unstructured absorber layers²⁰. However, nanostructured silicon photovoltaic cells with either radial^{4,8,10–12} or diffused^{13–16,18} p–n junctions show poor cell efficiency compared with commercially available wafer silicon photovoltaics whose efficiency can reach 15–21%. This Article addresses the reasons for the shortfall in nanostructured cell efficiency and describes routes for improvement.

Increased photocarrier recombination at the dramatically increased surface area of nanostructured silicon decreases the cell efficiency by reducing device short-circuit current J_{sc} , and open-circuit voltage V_{oc} . For example, in our laboratory's wafer silicon solar cells (with nanostructured antireflection surfaces made by gold-nanoparticle catalysed etching), we observed an increased recombination that dramatically reduces the collection of photocarriers generated by blue and green (that is, 350–600 nm) photons¹³. However, it was only possible to model the measured quantum

efficiency of these nanostructured cells by including an *ad hoc* 'dead layer' extending ~ 500 nm beneath the front surface, in which minority carrier lifetime is extremely low. This dead layer is roughly as thick as the nanoporous layer itself, and modelling with increased planar surface recombination alone was impossible. Most recently, we reported that blue quantum efficiency could be increased by decreasing the nanopore depth¹⁸, but this inevitably compromises the beneficial effects of the nanostructure for photon management.

To determine the recombination mechanisms in high-surface-area silicon solar cells, we fabricated diffused p–n junction solar cells in nanostructured silicon wafers, with various surface morphologies and areas. This model system mimics the excellent photoexcited charge separation in solar cells with a core–shell junction geometry but provides advantages in developing a fundamental understanding because aspects of the design and fabrication of radial p–n junction silicon solar cells, including uniform doping along the axis of the silicon wires²¹, are still poorly controlled and unoptimized¹¹. Nanopore formation and cell fabrication are described in detail in the Methods; however, the key points are that vertical nanopores are first formed by a metal-assisted etch^{3,12–14}, and that a subsequent anisotropic tetramethylammonium hydroxide (TMAH) etch controls the final surface morphologies and areas.

Photocarrier recombination in silicon nanostructures

Figure 1 compares cross-sectional scanning electron microscopy (SEM) images of the silicon nanostructures in the finished solar cells without any TMAH etch (Fig. 1a) and with a 30 s TMAH pore-widening modification (Fig. 1b). The unmodified pores (Fig. 1a) are vertically aligned cylinders with diameters ranging from ~ 30 to 100 nm; the pore depths appear to be random, with a maximum depth of ~ 480 nm. The 30 s TMAH modification decreases the nanostructured front surface area A^F by widening the pore diameters and linking pores to decrease their areal density. In addition, the modified pores in the finished solar cell (Fig. 1b) are slightly shallower (≤ 340 nm). As shown in Fig 1c, the surface area enhancement of nanostructured silicon over planar silicon, A^F/A_{proj} , decreases from 5.2 to 2.9 with a TMAH

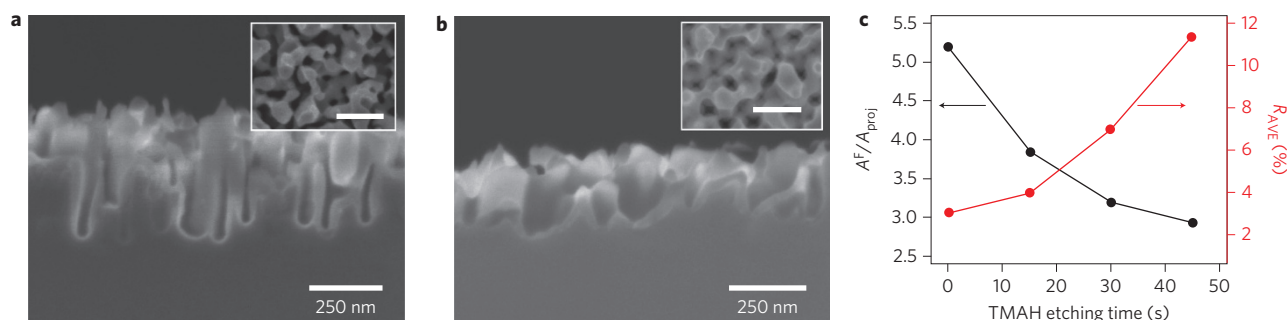


Figure 1 | Morphology and reflectance of nanostructured silicon solar cells. Silicon nanostructures were formed using metal-assisted etching. **a**, Cross-sectional SEM images of an unmodified silicon nanostructure solar cell. **b**, Cross-sectional SEM image of modified nanostructured silicon solar cells, treated with TMAH solution for 30 s after metal-assisted etching. The conformal layer with bright contrast in each cross-section is the SiO₂ passivation layer. Insets: plan-view SEM images (scale bars, 250 nm). $A^F/A_{proj} = 5.2$ (**a**) and 3.2 (**b**). **c**, Measured surface area enhancement ratio A^F/A_{proj} and the solar spectrum averaged reflectance R_{AVE} of silicon solar cell nanostructures as a function of TMAH etching time.

etching time of 45 s. Here, A_{proj} is the projected area of the nanostructures, equal to the planar area of the polished wafer. The TMAH etch increases the optical reflectance, R_{AVE} , from ~3 to 11%, as shown in Fig. 1c and discussed in Supplementary Section S1.

The transient photoconductance decay of excess carriers photogenerated in the solar cell (see Methods) can reveal how excess carriers recombine in various parts of the silicon absorber²². Figure 2a shows the effective carrier lifetime τ_{eff} of nanostructured silicon wafers with passivated n⁺-p junctions and four different nanostructure surface areas (controlled by TMAH etch time), as a function of sheet resistance R_s of the diffused n⁺ emitter (controlled by the diffusion time of doping carried out after the etches). Also shown is τ_{eff} of a polished silicon wafer versus R_s . As shown in Fig. 2a, τ_{eff} of the nanostructured silicon is strongly influenced both by the presence of the nanostructure and R_s . At each value of emitter R_s , τ_{eff} decreases as the surface area increases: in other words, nanostructured silicon with enhanced surface area promotes carrier recombination despite the thermal SiO₂ surface passivation layer. For example, with a 55 $\Omega \square^{-1}$ n⁺ emitter, which is typical of diffused junction solar cells, τ_{eff} decreases from 130 μ s for polished silicon to 71 μ s for a silicon wafer nanostructured with $A^F/A_{proj} = 5.2$ (black symbols).

Significantly, the value of the emitter R_s determines three different regimes of τ_{eff} behaviour, as indicated by the colour-coded regions in Fig. 2a. For a given silicon nanostructure (that is, at fixed surface area), τ_{eff} increases (Region I) as R_s increases from ~55 to ~100 $\Omega \square^{-1}$ and then saturates (Region II) as R_s increases further. Finally, τ_{eff} decreases (Region III) for the highest-resistivity emitters. For instance, silicon nanostructures with $A^F/A_{proj} = 3.2$ (blue symbols) show $\tau_{eff} = 84 \mu$ s for Region I, rising to $201 \pm 30 \mu$ s across all of Region II, and then falling to $132 \pm 2 \mu$ s in Region III. In contrast, the polished silicon wafer shows two distinctive regions (Region I and II) for τ_{eff} with only a slight decrease in Region III.

Generally, the τ_{eff} of minority carriers in silicon with a diffused emitter is expressed as $1/\tau_{eff} = 1/\tau_{bulk} + (S_{eff}^F + S_{eff}^B)/d$ (ref. 22), where τ_{bulk} is the bulk Shockley–Reed–Hall lifetime, S_{eff}^F and S_{eff}^B are the effective surface recombination velocities at the front and back surfaces, respectively, and d is wafer thickness (in our case, 300 μ m). Assuming that τ_{bulk} (~2 ms for our silicon wafers) does not change during solar cell processing and has negligible effect on the measured τ_{eff} ,

$$S_{eff}^F \approx \frac{d}{\tau_{eff}} - S_{eff}^B \quad (1)$$

for the nanostructured front surface. From our double-side polished wafer, S_{eff}^B is easily determined as $S_{eff}^F = S_{eff}^B \approx d/2\tau_{eff}$. Although

equation (1) describes a planar solar cell surface well, it treats recombination events in a nanostructure imprecisely, as if they are occurring in a projected planar geometry.

To analyse the effects of high surface area on the S_{eff}^F of nanostructured silicon, we propose a general expression for the measured effective lifetime in the case when recombination is localized at or very near the actual front surface:

$$\frac{1}{\tau_{eff}} = \frac{1}{\tau_{bulk}} + \left(S_{loc}^F \cdot \frac{A^F}{A_{proj}} + S_{eff}^B \right) / d \quad (2)$$

Equation (2) explicitly includes recombination terms reflecting the high surface area of the nanostructures at the front surface, and the back surface is still treated as a polished surface. Therefore, S_{eff}^F , determined experimentally from equation (1), is given by

$$S_{eff}^F \equiv S_{loc}^F \cdot \frac{A^F}{A_{proj}} \quad (3)$$

In equations (2) and (3), S_{loc}^F is the local effective surface recombination velocity at and very near the actual front surface and A^F/A_{proj} is the surface area enhancement ratio in Fig. 1c. S_{loc}^F in equations (2) and (3) parameterizes complicated local recombination kinetics in a region that follows the contours of the nanostructures closely, and includes surface and near-surface recombination. These mechanisms could include recombination through surface states as well as Auger recombination in the heaviest doped parts of the emitter very near the nanostructured surface. According to equation (3), if the local S_{loc}^F is independent of the scale of the silicon nanostructures, S_{eff}^F will display a linear dependence on A^F/A_{proj} , with a constant slope of S_{loc}^F .

Figure 2b plots the measured S_{eff}^F (determined from equation (1)) of the nanostructured silicon versus A^F/A_{proj} . Clearly, S_{eff}^F increases with increasing surface area for all Regions I, II and III. However, S_{eff}^F depends linearly on surface area only in the lightly doped Region III, with the fit extending even to the polished silicon data. The best fit for the Region III data in Fig. 2b gives $S_{loc}^F \approx 56 \text{ cm s}^{-1}$, which is nearly equal to the 53 cm s^{-1} we measured for the surfaces of double-side polished silicon. This validates our assumption that the local S_{loc}^F is independent of the nanostructure and is the same as on polished surfaces, at least for light doping. In Region III, the surface recombination associated with high surface area in the nanostructured silicon dominates other photocarrier recombination mechanisms. We note that the decrease of τ_{eff} with decreased doping in Region III of Fig. 2a stems, in part, from a reduction of the built-in E field that is essential to prevent injection of excess holes from the base to the front surface in the emitter²³.

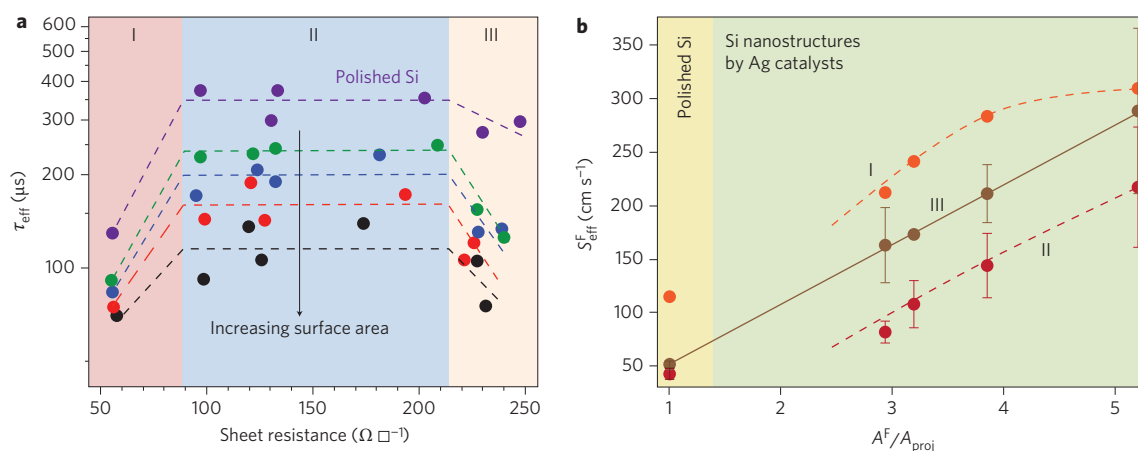


Figure 2 | Effective carrier lifetime and effective surface recombination velocity of polished and nanostructured silicon from photoconductance decay.

a, Effective carrier lifetime τ_{eff} of polished and nanostructured silicon, determined at carrier injection level $\Delta n \approx 1 \times 10^{15} \text{ cm}^{-3}$. The colour-coded symbols and dashed lines indicate the measured surface area enhancement ratio: black, red, blue and green symbols represent silicon nanostructures with $A^F/A_{\text{proj}} = 5.2$, 3.8, 3.2 and 2.9, respectively. Purple symbols represent polished silicon. Dashed lines are guides to the eye. Regions I, II and III delineate three different regimes of lifetime determined by sheet resistance. **b**, Effective surface recombination velocity S_{eff}^F with dashed lines as guides to the eye. The solid brown line is a linear fit to Region III data. Colour-coded symbols and lines indicate the emitter doping strength: orange, maroon and brown for Regions I, II and III, respectively.

Figure 2b also shows that the S_{eff}^F of nanostructured silicon with the most heavily doped emitters (Region I) becomes nearly independent of total surface area when A^F/A_{proj} is larger than ~ 3.8 . This implies that for heavy emitter doping and a highly nanostructured surface, recombination is not dominated by a local surface process (for example, recombination is not mainly through surface defects).

For doping concentration higher than $1 \times 10^{18} \text{ cm}^{-3}$ in silicon, Auger recombination normally dominates the recombination process and causes low lifetime²³ and high S_{eff}^F in heavily doped emitters^{24,25}. As shown in Fig. 2b, S_{eff}^F of our polished silicon in Region I is more than twice that in Region II due to this increased Auger recombination. In the moderately doped Region II, S_{eff}^F deviates slightly from the linear area dependence and does not extrapolate to that of the polished silicon; in other words, the recombination mechanisms of both Regions I and III cannot be neglected.

On a nanostructured silicon surface, the diffused phosphorus dopant profile will be significantly different from that on polished silicon for a given junction formation condition. Phosphorus dopants diffuse in from the entire surface of the nanostructure. The diffused junction depth in a polished wafer ($>500 \text{ nm}$) after annealing at 850°C is an order of magnitude bigger than the lateral feature size of silicon nanostructures ($\sim 50 \text{ nm}$). Therefore, as shown schematically in Fig. 3, the phosphorus concentration in a diffused nanostructured wafer is constant and close to the surface peak concentration throughout the entire depth of the nanostructures.

High Auger recombination inside a heavily doped, nanostructured emitter layer prevents photocarrier diffusion and suppresses recombination at surface defects. The effective recombination rate of the nanostructured silicon will then increase with the volume of the heavily doped silicon associated with the nanostructures, rather than depending directly on surface area. This is seen in the lack of surface area dependence for $A^F/A_{\text{proj}} > 3.8$ in Region I of Fig. 2b. For silicon nanostructures with $A^F/A_{\text{proj}} < 3.8$ in Region I, the volume of the heavily doped silicon nanostructures is smaller, and so is S_{eff}^F . In contrast, when we form an n^+ junction with low surface peak concentration and shallow junction depth (Regions II and III), Auger recombination is suppressed and lifetime depends primarily on surface recombination and therefore A^F (Fig. 2a).

The lifetime data clearly indicate that there are two parallel recombination channels in the emitter of a solar cell—Auger and surface recombination—as depicted schematically in Fig. 3.

Compared with a planar cell, nanostructuring worsens the Auger and surface recombination channels by altering the doping profile and increasing the surface area, respectively. In the highly doped Region I, the Auger recombination channel dominates via excess doping through the nanostructured surface area. In the low-doped Region III, the surface recombination channel dominates because of increased surface defects and area; keeping the emitter doping low shuts off the Auger recombination channel. In the medium-doped Region II, both Auger and surface state channels are important in determining surface recombination.

Charge collection efficiency in silicon nanostructures

To determine the charge collection efficiency of photons absorbed in and near the nanostructures and better understand the

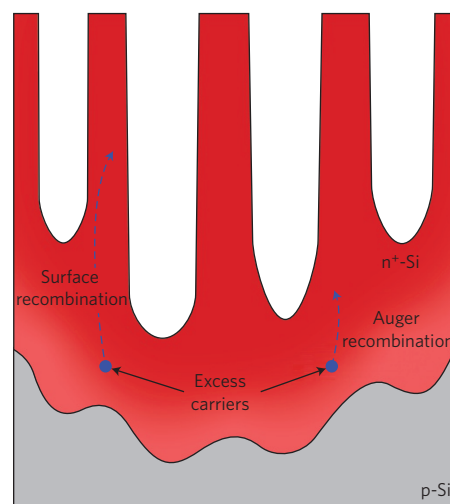


Figure 3 | Schematic of excess carrier recombination mechanisms in the silicon nanostructure.

Photogenerated excess carriers (blue dots) in the n^+ -Si nanostructures (red regions in the figure) dissipate by parallel recombination channels: Auger and surface recombination. If Auger recombination is the dominant recombination process, the high surface area has a secondary effect on the recombination rate. (Note that the schematic is not drawn to scale.)

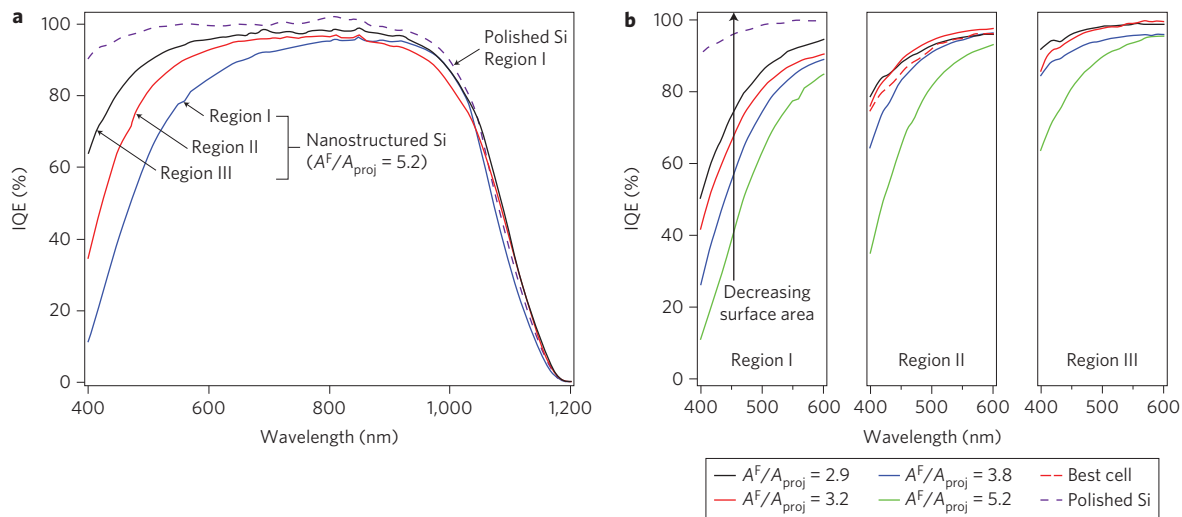


Figure 4 | IQE of nanostructured silicon solar cells. **a**, IQE of nanostructured silicon solar cells in Regions I ($R_s \approx 55 \Omega \square^{-1}$), II ($R_s \approx 123 \Omega \square^{-1}$) and III ($R_s \approx 235 \Omega \square^{-1}$), each with a surface area enhancement ratio of 5.2. Dashed line is the IQE of a polished silicon solar cell in Region I ($R_s \approx 55 \Omega \square^{-1}$). **b**, Blue response of nanostructured silicon solar cells in Regions I, II and III, with surface area A^F/A_{proj} varying from 2.9 to 5.2 (solid lines). The purple dashed curve in Region I represents the response of a polished cell. The dashed red curve in Region II is the IQE of our best nanostructured solar cell (Fig. 5).

recombination processes, we measured the spectral dependence of internal quantum efficiency (IQE). Figure 4a compares the IQEs of identically nanostructured silicon solar cells ($A^F/A_{\text{proj}} = 5.2$) with doping in Regions I ($R_s \approx 55 \Omega \square^{-1}$), II ($R_s \approx 123 \Omega \square^{-1}$) and III ($R_s \approx 235 \Omega \square^{-1}$) to the IQE of polished silicon in Region I. The nanostructured silicon in the heavily doped Region I has an extremely poor IQE for photons absorbed within $2 \mu\text{m}$ of the surface, which corresponds to incident wavelengths from 400 to 600 nm. For example, the IQE at 400 nm is only 11% for nanostructured silicon, compared with 90.5% for polished silicon. This poor blue spectral response is observed in most nanostructured solar cells. It limits the J_{sc} and overall solar cell efficiency, and is usually attributed to increased surface recombination processes at the high surface area of the nanostructures. However, as discussed above, such increased recombination actually results from the high Auger recombination rate associated with the formation of a far thicker and more heavily doped emitter in nanostructured silicon than in polished silicon under the same doping conditions. Photogenerated charges within and just below the heavily doped silicon nanostructure have little chance either of being collected or of recombining at the actual surface. In addition, because many photons with longer wavelengths are also absorbed in the Auger-dominated silicon nanostructures, the IQE is significantly degraded for photons with wavelengths from 600 nm to 900 nm compared with polished silicon (Fig. 4a). By reducing doping to suppress this Auger recombination process, the IQE of the nanostructured silicon solar cells is dramatically improved. As shown in Fig. 4a, the IQE of nanostructured silicon in Region III increases to 63.8% at 400 nm and reaches 90–98% from 500 to 900 nm, simply by decreasing the phosphorus content (increasing R_s) in nearly identical nanostructures.

Figure 4b clarifies the effect of surface area on the blue IQE where different recombination mechanisms dominate. The IQE of a surface recombination-dominated silicon nanostructure (lightly doped Region III) is improved by decreasing the surface area, until silicon with $A^F/A_{\text{proj}} \leq 3.8$ the IQE reaches above 85% at 400 nm. This blue IQE is nearly identical to that of polished silicon (dashed purple, left panel) in Region I. Indeed, between 400 and 600 nm, the IQE of the $A^F/A_{\text{proj}} \approx 3.8$ nanostructured cell shows a loss of only $\sim 1.1 \text{ mA cm}^{-2}$ in J_{sc} as a result of the doped nanostructures, compared with an ideal silicon absorber.

This is a small loss compared with the beneficial impact of reducing reflection through nanostructuring. In contrast, the application of low-surface-area nanostructures improves the 400 nm IQE only to a small extent in the heavily doped Region I (up to 50.5% for $A^F/A_{\text{proj}} = 2.9$), because the Auger recombination depends primarily on the depth and volume of the heavily phosphorus-doped nanostructures rather than on their surface area.

18.2%-efficient nanostructured wafer silicon solar cell

Figure 5 shows the J - V curve of our best nanostructured black-silicon solar cell, as measured independently by NREL's ISO-certified photovoltaics testing laboratory. Both Auger recombination and surface recombination are simultaneously reduced by applying a slightly modified fabrication procedure (see Methods). An SEM image of our best nanostructured silicon solar cell is shown in the

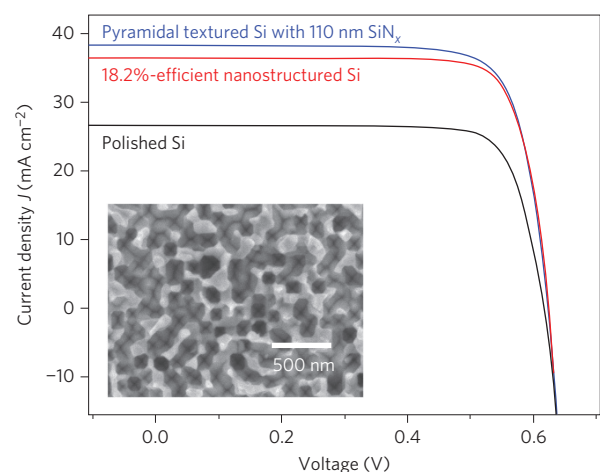


Figure 5 | J - V curves of 18.2%-efficient nanostructured black silicon, polished silicon and pyramid-textured silicon with an SiN_x antireflection coating under AM 1.5G illumination. The device area of the 18.2%-efficient nanostructured silicon solar cell shown here is 0.8081 cm^2 ; the areas of others are 1 cm^2 . Only the measurement of the nanostructured cell was taken on NREL's ISO-certified equipment; a different calibrated simulator was used to measure the other two cells. Inset: plan-view SEM image of the cell.

Table 1 | Solar cell efficiency and J - V parameters of the silicon solar cells of Fig. 5.

	V_{oc} (mV)	J_{sc} (mA cm ⁻²)	FF (%)	Efficiency (%)
Polished silicon	617	26.62	79.6	13.1
Pyramid textured silicon with 110 nm SiN _x	624	38.26	78.1	18.6
Our best nanostructured silicon	628	36.45	79.6	18.2

inset in Fig. 5. The fabricated cell has $R_s \approx 129 \Omega \square^{-1}$ (Region II), and an effective lifetime of $\sim 198 \mu\text{s}$. The cell antireflection is provided by the graded index of refraction in the nanostructures; there is no additional antireflection coating. This nanostructured silicon solar cell has $V_{oc} = 0.628 \text{ V}$, $J_{sc} = 36.45 \text{ mA cm}^{-2}$ and fill factor (FF) = 79.6%, with 18.2% efficiency under AM 1.5G illumination.

For qualitative comparison, Fig. 5 also presents the J - V curves of a polished solar cell with no antireflection and a cell with the industry-standard pyramid texture and antireflection coating (see Methods). Table 1 summarizes the V_{oc} , J_{sc} , FF and efficiency values of the solar cells shown in Fig. 5. The silicon nanostructure antireflection enhances optical absorption and increases J_{sc} by $\sim 10 \text{ mA cm}^{-2}$ compared with the polished silicon solar cell, and leads to an absolute 5.1% increase in efficiency. Moreover, the efficiency of our nanostructured silicon solar cell is comparable to that of industry-standard silicon solar cells made in our laboratory. This nanostructured solar cell has the advantage of lowering plant capital investment and reducing processing cost by eliminating the need for vacuum-based antireflection coating equipment.

Unlike previous nanostructured solar cells, our best nanostructured cell is not primarily limited by the poor blue response associated with the nanostructures (a loss of only 1.16 mA cm^{-2} from 400 to 600 nm, as seen in the dashed red line in Fig. 4b); rather, it suffers from a 4.6% reflectance loss atypical of such black-silicon cells (see reflectance spectrum in Supplementary Section S2) and a poorly optimized aluminium back contact. We estimate that optimization of the nanostructure for antireflection together with excellent back passivation in a point contact geometry could raise the efficiency of a nanostructured silicon solar cell to above 20% (for a more detailed analysis, see Supplementary Section S3). Further reductions in cost are expected if the high cost of silicon wafers is avoided by incorporating larger light-trapping nanostructures, together with these small nanopores, in thin crystalline silicon film solar cells⁷.

Our results also suggest important design rules for efficient solar cells using high-aspect-ratio nano- and microstructured semiconductors with radial p-n junctions. Doping and surface passivation schemes must be carefully designed to minimize the Auger and surface recombination aggravated by high-aspect-ratio structures (for a detailed discussion, see Supplementary Section S4). Furthermore, electrical contact techniques must be designed to achieve high FF values, despite the high sheet resistance needed to suppress emitter Auger recombination in nano- and microstructured solar cells. Our test cells suffer a drop in FF from 79.3 to 75.9% as R_s increases from ~ 55 (Region I) to $\sim 235 \Omega \square^{-1}$ (Region III), even though the cell of Fig. 5 retains an FF of $\sim 79.6\%$.

In summary, we have demonstrated that there are two competing charge recombination processes in nanostructured silicon solar cells, with the dominant mechanism depending on p-n junction formation conditions and the amount of nanostructured surface area. Contrary to common belief, we have quantitatively shown that it is the Auger recombination process, and not simply surface recombination associated with high surface area, that limits the photogenerated charge collection and cell efficiency of most

nanostructured silicon solar cells. This Auger recombination is caused by excessive doping related to in-diffusion through the high surface area of the silicon nanostructures. By suppressing Auger recombination with light and shallow doping and simultaneously controlling surface area, we have demonstrated nanostructured wafer black-silicon solar cells, with no additional antireflection coating, that have a nearly ideal blue spectral response and a confirmed 18.2% efficiency under simulated AM 1.5G illumination.

Methods

Sample fabrication. Float-zone grown, 300- μm -thick, p-type (100)Si wafers (boron doped, $2.8 \Omega \text{ cm}$) with double-side polished surfaces were used for this work. Silicon nanostructures at the front surface were formed using a two-step metal-assisted etching technique, as described elsewhere²⁶. The backside of the silicon wafers was protected by a photoresist (AZ1518) during etching. Silver nanoparticles were electrolessly deposited on the silicon wafers in a mixed solution of 1 mM AgNO₃ and 0.5 vol% HF for 90 s at room temperature. Nanoporous silicon was formed by preferentially etching silicon in the [100] direction in the vicinity of silver nanoparticles, in a mixed solution of 12.5 vol% HF, 3 vol% H₂O₂ and deionized (DI) water for 20 s at room temperature. After photoresist removal from the backside using acetone and isopropanol, the silicon nanostructures were treated with concentrated HNO₃ for 3 min to remove silver nanoparticles at the bottom of the pores, followed by a DI water rinse for 3 min, and then immersed in 5 vol% HF for 90 s at room temperature to remove the SiO₂ formed during HNO₃ treatment. Samples were then etched for various times in 1 vol% TMAH solution at room temperature to decrease the surface area of the silicon nanostructures; the results are described in detail in the text accompanying Figs 1 to 4.

Conventional diffused-junction silicon solar cell processing was used to fabricate nanostructured silicon solar cells, as described elsewhere¹³. After standard RCA cleaning (as developed at Radio Corporation of America), the n⁺-emitter was formed by phosphorus diffusion using a POCl₃ liquid source at 850 °C for various diffusion times to control R_s . The phosphosilicate glass that formed during POCl₃ diffusion was removed with 5 vol% HF. A SiO₂ passivation layer was then formed by thermal oxidation at 850 °C for 30 min to passivate the surfaces. Back metal contacts were made by applying aluminium paste (Ferro FX 053-038) and alloying at 800 °C, after removing the SiO₂ passivation layer at the back surface using a dilute HF solution. For the front metal contact, the desired grid pattern was formed in SiO₂ on the front surface by photolithography and etching in dilute HF. A Ti/Ag/Pd contact grid was then formed by electron-beam evaporation and metal liftoff processes.

For the cell with the J - V curve shown in Fig. 5, there was no TMAH etch before emitter formation. Instead, a 60 s etch at room temperature in 1 vol% TMAH solution was used after n⁺-emitter formation to reduce surface phosphorus doping concentration and surface area. All other processes were unaltered. The industry-type cell on pyramid textured silicon had doping in Region I followed by a 110-nm-thick SiN_x antireflection layer made by plasma-enhanced chemical vapour deposition.

Sample characterization. The samples used to measure surface area were studied after oxide passivation and without undergoing any metal contact formation steps. The surface area of the nanostructured silicon was determined by carefully measuring the mass of the thermal SiO₂ passivation layer before and after SiO₂ removal with HF. The two values were subtracted to obtain the mass of SiO₂ removed. A polished silicon sample of known area had been weighed similarly before and after SiO₂ removal. The measured SiO₂ mass was then converted to nanostructured surface area by assuming the thickness of the SiO₂ on the nanostructures was the same as the thickness on the polished silicon. Although this assumption neglects the fact that the silicon oxidation kinetics depends on various factors including crystallographic orientation, surface roughness and the curvature of the silicon nanostructures^{27,28}, we have studied selected SEM images of samples and estimate that our reported oxide thickness has an absolute error of $\sim 10\%$. The relative errors among the various samples should be much smaller.

Effective carrier lifetime was measured after surface passivation, using the transient photoconductance decay method²² (WCT-120, Sinton Consulting) at an injection level of $\Delta n \approx 1 (\pm 0.5) \times 10^{15} \text{ cm}^{-3}$. In Regions II and III of Fig. 2, error bars were determined by calculating the standard deviation of all data points at a given surface area; some error bars are contained within the plotted point. In Region I, there is a single data point for each surface area. Sheet resistance was measured using a four-point probe on the polished back surface of front-nanostructured silicon, before metal contact formation. We measured the total reflectance spectra with a Varian Cary 6000i spectrometer using an integrating sphere, after aluminium back contact formation, but before the front grid was formed. This measured total reflectance R was converted to the total absorption $(1-R)$ and used to extract the IQE from the external quantum efficiency (EQE) measurement; the light beam in our EQE measurement equipment fits in the $1 \text{ mm} \times 5 \text{ mm}$ space between the front metal grid fingers so that absorption or reflection by the front metal contact is precluded. International Organization for Standards (ISO) certified solar cell performance was measured at AM 1.5G

illumination by the Solar Cell/Module Performance Group at NREL. In Fig. 5, only the nanostructured black-silicon solar cell efficiency was independently confirmed by NREL's ISO certified photovoltaics testing laboratory; calibrations of the different simulators used may differ slightly.

Received 11 June 2012; accepted 27 August 2012;
published online 30 September 2012

References

- Stephens, R. B. & Cody, G. D. Optical reflectance and transmission of a textured surface. *Thin Solid Films* **45**, 19–29 (1977).
- Koynov, S., Brandt, M. S. & Stutzmann, M. Black nonreflecting silicon surfaces for solar cells. *Appl. Phys. Lett.* **88**, 203107 (2006).
- Branz, H. M. *et al.* Nanostructured black silicon and the optical reflectance of graded-density surfaces. *Appl. Phys. Lett.* **94**, 231121 (2009).
- Garnett, E. & Yang, P. D. Light trapping in silicon nanowire solar cells. *Nano Lett.* **10**, 1082–1087 (2010).
- Kelzenberg, M. D. *et al.* Enhanced absorption and carrier collection in Si wire arrays for photovoltaic application. *Nature Mater.* **9**, 239–244 (2010).
- Han, S. E. & Chen, G. Optical absorption enhancement in silicon nanohole arrays for solar photovoltaics. *Nano Lett.* **10**, 1012–1015 (2010).
- Branz, H. M. *et al.* Hot-wire chemical vapor deposition of epitaxial film crystal silicon for photovoltaics. *Thin Solid Films* **519**, 4545–4550 (2011).
- Tian, B. Z. *et al.* Coaxial silicon nanowires as solar cells and nanoelectronic power sources. *Nature* **449**, 885–888 (2007).
- Weisse, J. M., Kim, D. R., Lee, C. H. & Zheng, X. L. Vertical transfer of uniform silicon nanowire arrays via crack formation. *Nano Lett.* **11**, 1300–1305 (2011).
- Boettcher, S. W. *et al.* Energy-conversion properties of vapor-liquid-solid-grown silicon wire-array photocathodes. *Science* **327**, 185–187 (2010).
- Putnam, M. C. *et al.* Si microwire-array solar cells. *Energy Environ. Sci.* **3**, 1037–1041 (2010).
- Garnett, E. C. & Yang, P. D. Silicon nanowire radial p–n junction solar cells. *J. Am. Chem. Soc.* **130**, 9224–9225 (2008).
- Yuan, H. C. *et al.* Efficient black silicon solar cell with a density-graded nanoporous surface: optical properties, performance limitations, and design rules. *Appl. Phys. Lett.* **95**, 123501 (2009).
- Peng, K. Q. *et al.* Aligned single-crystalline Si nanowire arrays for photovoltaic applications. *Small* **1**, 1062–1067 (2005).
- Sai, H. *et al.* Wide-angle antireflection effect of subwavelength structures for solar cells. *Jpn. J. Appl. Phys.* **46**, 3333–3336 (2007).
- Yoo, J., Yu, G. & Yi, J. Black surface structures for crystalline silicon solar cells. *Mater. Sci. Eng. B* **159–160**, 333–337 (2009).
- Her, T. H. *et al.* Microstructuring of silicon with femtosecond laser pulses. *Appl. Phys. Lett.* **73**, 1673–1675 (1998).
- Toor, F. *et al.* Multi-scale surface texture to improve blue response of nanoporous black silicon solar cells. *Appl. Phys. Lett.* **99**, 1030501 (2011).
- Garnett, E. C., Brongersma, M. L., Cui, Y. & McGehee, M. D. Nanowire solar cells. *Annu. Rev. Mater. Res.* **41**, 269–295 (2011).
- Kayes, B. M., Atwater, H. A. & Lewis, N. S. Comparison of the device physics principles of planar and radial p–n junction nanorod solar cells. *J. Appl. Phys.* **97**, 114302–114311 (2005).
- Koren, E. *et al.* Nonuniform doping distribution along silicon nanowires measured by Kelvin probe force microscopy and scanning photocurrent microscopy. *Appl. Phys. Lett.* **95**, 092105 (2009).
- Aberle, A. G. *Crystalline Silicon Solar Cells: Advanced Surface Passivation and Analysis* (Centre for Photovoltaic Engineering, University of New South Wales, 1999).
- Green, M. A. *Solar Cells: Operating Principles, Technology, and System Applications* (Prentice-Hall, 1982).
- King, R. R., Sinton, R. A. & Swanson, R. M. Studies of diffused phosphorus emitters—saturation current, surface recombination velocity, and quantum efficiency. *IEEE Trans. Electron. Dev.* **37**, 365–371 (1990).
- Cuevas, A., Basore, P. A., Girault-Matlakowski, G. & Dubois, C. Surface recombination velocity of highly doped n-type silicon. *J. Appl. Phys.* **80**, 3370–3375 (1996).
- Huang, Z. P. *et al.* Metal-assisted chemical etching of silicon: a review. *Adv. Mater.* **23**, 285–308 (2011).
- Kao, D.-B., McVittie, J. P., Nix, W. D. & Saraswat, K. C. Two-dimensional thermal oxidation of silicon-I. Experiments. *IEEE Trans. Electron. Dev.* **34**, 1008–1017 (1987).
- Liu, H. I. *et al.* Self-limiting oxidation for fabricating sub-5 nm silicon nanowires. *Appl. Phys. Lett.* **64**, 1383–1385 (1994).

Acknowledgements

The authors thank B. To of NREL for assistance with SEM. The authors are grateful to F. Toor and M.R. Page of NREL for many helpful discussions and T. Buonassisi of MIT for important insight into the role of Auger recombination. This work was supported by a DOE American Recovery and Reinvestment Act (ARRA) Photovoltaic Supply Chain and Crosscutting Technologies grant (contract no. DE-AC36-08GO28308).

Author contributions

J.O. conceived and designed the study to answer the questions posed jointly by J.O., H.-C.Y. and H.M.B. J.O. performed the experiments and analysed the data. J.O. and H.M.B. co-wrote the paper. All authors discussed the results and improved the manuscript.

Additional information

Supplementary information is available in the online version of the paper. Reprints and permission information is available online at <http://www.nature.com/reprints>. Correspondence and requests for materials should be addressed to J.O.

Competing financial interests

The authors declare no competing financial interests.